

1 Uranus' aurorae past equinox

L. Lamy¹, R. Prangé¹, K. C. Hansen², C. Tao³, S. W. H. Cowley⁴, T.

Stallard⁴, H. Melin⁴, N. Achilleos⁵, P. Guio⁵, S. V. Badman⁶, T. Kim⁷,

N. Pogorelov⁷

Author Manuscript

This is the author manuscript accepted for publication and has undergone full peer review but has not been through the copyediting, typesetting, pagination and proofreading process, which may lead to differences between this version and the Version of Record. Please cite this article

as doi: [10.1002/2017JA023918](https://doi.org/10.1002/2017JA023918) March 7, 2017, 9:31pm

D R A F T

1. Abstract

2 The aurorae of Uranus were recently detected in the far ultraviolet with the Hubble
3 Space Telescope (HST) providing a new, so far unique, means to remotely study the
4 asymmetric Uranian magnetosphere from Earth. We analyze here two new HST Uranus
5 campaigns executed in Sept. 2012 and Nov. 2014 with different temporal coverage and

¹LESIA, Obs. de Paris, CNRS, UPMC,
Univ. Paris Diderot, Meudon, France

²Department of Atmospheric, Oceanic
and Space Sciences, University of Michigan,
Ann Arbor, Michigan, USA.

³NICT, Tokyo, Japan

⁴Department of Physics and Astronomy,
University of Leicester, Leicester, UK

⁵University College London, Mullard
Space Science Laboratory, Dorking, UK

⁶Lancaster University, Lancaster, UK

⁷Center for Space Plasma and Aeronomic
Research, University of Alabama,
Huntsville, USA

under variable solar wind conditions numerically predicted by three different MHD codes. Overall, HST images taken with the Space Telescope Imaging Spectrograph reveal auroral emissions in three pairs of successive images (one pair acquired in 2012 and two in 2014), hence six additional auroral detections in total, including the most intense Uranian aurorae ever seen with HST. The detected emissions occur close the expected arrival of interplanetary shocks. They appear as extended spots at southern latitudes, rotating with the planet. They radiate 5-24 kR and 1.3-8.8 GW of ultraviolet emission from H₂, last for tens of minutes and vary on timescales down to a few seconds. Fitting the 2014 observations with model auroral ovals constrains the longitude of the southern (northern) magnetic pole to $104 \pm 26^\circ$ ($284 \pm 26^\circ$) in the Uranian Longitude System. We suggest that the Uranian near-equinoctial aurorae are pulsed cusp emissions possibly triggered by large-scale magnetospheric compressions.

2. Introduction

The Hubble Space Telescope (HST) recently succeeded in re-detecting the Far UltraViolet (FUV) aurorae of Uranus in 2011 and then in 1998 [*Lamy et al.*, 2012] (hereafter L12), long after their discovery by the UV Spectrometer (UVS) of Voyager 2 in 1986 [*Broadfoot et al.*, 1986]. These detections included the first images of Uranus' aurorae and provided a new means to remotely investigate the poorly known magnetosphere of Uranus from Earth, awaiting for any future in situ exploration [*Arridge et al.*, 2011]. This asymmetric magnetosphere has no equivalent in the solar system, with a spin axis close to the ecliptic plane, a 84-year revolution period which carried Uranus from Solstice in 1986 to Equinox in 2007, a fast spin period of 17.24 ± 0.01 h and a 59° tilt between the magnetic and the spin axes [*Ness et al.*, 1986]. The geometry of the solar wind-magnetosphere interaction

28 thus dramatically evolves over timescales ranging from a quarter of a rotation (hours) to
29 seasons (decades).

30 The 2011 HST observations were scheduled to sample the arrival at Uranus of a se-
31 ries of successive interplanetary shocks (displayed in Figure 1b), tracked through in situ
32 solar wind measurements near Earth and numerically propagated to Uranus with an up-
33 dated version of the Michigan Solar Wind Model (mSWiM), validated up to Saturn's
34 orbit [Zieger and Hansen, 2008]. The observations acquired with the Space Telescope
35 Imaging Spectrograph (STIS) yielded positive detections of auroral signal in two images
36 (out of eight) analyzed by L12 and one spectrum studied by Barthélémy *et al.* [2014],
37 and brought the first insights onto the Uranian magnetosphere near Equinox. The im-
38 ages revealed isolated auroral spots on 16 and 29 Nov. 2011 (gray arrows in Figure 1b),
39 lasting for a few min, radiating a few kilo-Rayleighs (kR) over the observed FUV range.
40 They were precisely colocated, rotationally phased in longitude and at -10° latitude.
41 Their occurrence near times of predicted increases of solar wind dynamic pressure (up to
42 0.01 nPa) suggested that the solar wind could play a significant role in driving dayside
43 auroral bursts. A STIS spectrum taken immediately after the STIS 29 Nov. 2011 image
44 revealed auroral H_2 emission, radiating in average 650 R between 70 nm and 180 nm over
45 the portion of the disc covered by the slit.

46 The re-analysis of STIS images of Uranus taken in 1998, in a configuration interme-
47 diate between Solstice and Equinox, yielded an additional detection during quiet solar
48 wind conditions (gray arrow in Figure 1a). Although fainter and closer to the detection
49 threshold than in 2011, the 1998 aurorae were seen in both hemispheres simultaneously
50 and more spatially extended along ring-like structures reminiscent of partial auroral ovals.

51 The emissions detected with HST contrasted with the Earth-like aurorae discovered by
52 UVS at Solstice. The latter were clustered on the nightside, mainly around the southern
53 magnetic pole along magnetotail longitudes, and radiated up to 3-7 GW in the H Ly α line
54 and in the H₂ bands ≤ 116 nm, *i.e.* roughly twice as much over the full 70-180 nm H₂ range
55 [Herbert and Sandel, 1994]. The variation of auroral characteristics along the Uranian
56 orbit thus provides a diagnostic of the solar wind/magnetosphere interaction at very
57 different timescales, which L12 assigned to changes of the magnetospheric configuration,
58 through particle acceleration mechanisms yet to be identified.

59 Two recent studies investigated possible origins of the observed auroral precipitations.
60 Cowley [2013] discussed the configuration of the Uranian magnetosphere at Equinox which
61 inhibits the formation of a magnetotail. Under such conditions, the Uranian magneto-
62 sphere appears unable to drive bright, long-lasting auroral storms such as those observed
63 at the Earth or Saturn induced by sudden magnetospheric compressions. Masters [2014]
64 modelled magnetopause reconnection at both Solstice and Equinox using Voyager 2 solar
65 wind parameters and concluded that dayside reconnection is in general less favorable at
66 Uranus than at inner planets, at Equinox than at Solstice, and predicted highly dynamic
67 reconnection sites.

68 In this article, we analyze two new HST campaigns executed in Sept. 2012 and Nov.
69 2014 with different temporal coverage and under variable solar wind conditions (section
70 3). The images provide six additional detections of Uranus aurorae, whose properties
71 display both similarities and differences with those of auroral emissions detected in 2011
72 (section 4). All Uranian aurorae seen by HST are then discussed together to investigate
73 any possible control by the solar wind and/or by the planetary rotation (section 5).

3. Dataset

3.1. HST observations

74 Following the Nov. 2011 HST campaign, two subsequent HST programs were executed
75 in Sept. 2012 and Nov. 2014, while Uranus gradually moved away from the 2007 Equinox.
76 These two programs consisted of a total of 19 HST visits, each one lasting 1 orbit, which
77 mainly used the Space Telescope Imaging Spectrograph (STIS, 17 orbits) but also the
78 Advanced Camera for Surveys (ACS, 1 orbit) and the Cosmic Origin Spectrograph (COS, 1
79 orbit)¹. All the STIS and COS observations were acquired with the time-tag mode, which
80 provides the arrival time of photons recorded on the MAMA detector at a 125 microsec
81 time resolution. In this article, we analyze the STIS data obtained along 13 imaging
82 orbits. We left aside ACS images which, as in L12, did not bring positive results. STIS
83 spectra were already analyzed by [Barthélémy *et al.*, 2014], while the analysis of COS
84 data is beyond the scope of this study. Each STIS imaging orbit was made of a pair
85 of consecutive images taken with the Far-UV MAMA (Multi-Anode Microchannel Array)
86 detector using the clear filter 25MAMA (137 nm central wavelength, 32 nm FWHM) which
87 spans H₂ bands and H Ly- α , and the Strontium Fluoride filter F25SrF₂ (148 nm central
88 wavelength, 28 nm FWHM) which rejects wavelengths shortward of 128 nm, including H
89 Ly- α .

90 The 2012 program was aimed at carefully sampling the rotational dynamics of auroral
91 processes in order to assess the influence of rotation on the magnetosphere/solar wind
92 interaction. The observations included 7 STIS imaging orbits spread from 27 to 29 Sept.
93 2012 over three consecutive planetary rotations, hence providing an excellent longitudinal

94 coverage. This interval matched a modest increase of solar wind dynamic pressure (Figure
95 1c).

96 The main goal of the 2014 program, obtained with director's discretionary time, was to
97 track the auroral response to two episodes of powerful interplanetary shocks characterized
98 by large fronts of dynamic pressure at Uranus (Figure 1d) up to or beyond 0.02 nPa
99 (depending on the solar wind model, see section 3.3), twice as large as in 2011 and thus
100 the largest ever sampled by both HST and Voyager 2. The observations included 6 STIS
101 imaging orbits distributed from 1 to 5 Nov. and from 22 to 24 Nov.

3.2. Image processing

102 The data were processed exactly as in L12 with the simple, robust two-steps pipeline
103 described below.

104 The STIS images were calibrated through the Space Telescope Science Institute pipeline
105 and corrected for any geocoronal contamination, by subtracting to all pixels a constant
106 offset intensity estimated beyond the disc. Indeed, F25MAMA images are highly sensitive
107 to contamination at H Ly- α and the oxygen OI 130.4 nm multiplet, but even F25SrF₂
108 images can be affected by strong oxygen lines. The level of contamination was variable
109 with time, resulting in a variable background level of STIS exposures. We then subtracted
110 to each image an empirical model of disc background of solar reflected emission. This
111 background model was built from a median image, derived separately for 25MAMA and
112 F25SrF₂ filters and for each HST campaign, before to be fitted to and subtracted from
113 each individual image.

114 Although some of the images used to build our empirical background possibly include
115 the auroral emissions we are looking for, the derived model is generally excellent, as the

116 location of auroral spots far from the rotational poles together with their short lifetime
117 renders it a priori unlikely to observe auroral signal exactly at the same position across
118 the planetary disc in different images. This was a posteriori confirmed by the different
119 location of detected auroral signal presented in section 4. The empirical background
120 models were built for the 2012 and 2014 campaigns from a set of 7 and 6 images taken
121 in each filter, respectively. The statistics was thus fair, but insufficient to smooth out
122 spatial inhomogeneities.

123 Therefore, we also used an alternate numerical background model of background built
124 with Minnaert functions [*Vincent et al.*, 2000] fitted to the disc emission of each image
125 and convolved by the STIS point spread function. This model, although less physical,
126 is smooth and well suited to track isolated auroral features. Hereafter, we display im-
127 ages processed with the empirical background, but we required auroral signatures to be
128 detected with both kinds of background models to be considered as positive detections.

129 Each background-subtracted image was then smoothed over a 5×5 pixels averaging filter
130 to increase the signal-to-noise ratio (SNR). This choice, already used by L12, was checked
131 by varying the size of the averaging filter and found to provide the best compromise
132 between increasing the SNR and preserving the spatial resolution.

133 The processed images in counts were ultimately transposed into physical units of kR and
134 GW of unabsorbed H₂ emission over 70-180 nm by using the conversion factors described
135 in [*Gustin et al.*, 2012]. This enables one to compare brightnesses derived with different
136 filters and more largely with different instrumentation.

3.3. Solar wind models

137 In L12, we used solar wind parameters at Uranus numerically propagated from the
 138 Earth orbit out to Uranus by one single MHD model, namely the Michigan Solar Wind
 139 Model (mSWiM) [Zieger and Hansen, 2008]. In the present study, we used the results
 140 of three different codes : mSWiM (1D), the Tao model (1D) [Tao et al., 2005] and the
 141 Multi-scale Fluid-kinetic Simulation Suite (3D, MS-FLUKSS) [Pogorelov et al., 2014], all
 142 using near-Earth solar wind in situ observations provided by NASA/GSFC's OMNI 1h
 143 averaged data set through OMNIWeb [?]. The results of these models are displayed by
 144 black, blue and orange lines in Figure 1, respectively. They are described in more details
 145 in appendix A by historical order of use and compared to infer their limitations. Overall,
 146 we estimate a typical uncertainty of ± 3 days on the dynamic pressure fronts at Uranus.

147 As only MS-FLUKKS has been validated yet in the outer heliosphere by the comparison
 148 of predicted parameters with in situ plasma measurements of Ulysses, Voyager and New
 149 Horizons missions [Kim et al., 2016], the MS-FLUKKS results (orange lines in Figures 1
 150 and 5) are hereafter taken as a primary reference to which the mSWiM and Tao results
 151 are compared.

4. Average properties of auroral structures

152 Simple criteria were used to identify auroral signatures : the emission region must
 153 reach or extend beyond a 4×4 pixels box with intensities per pixel exceeding 3 standard
 154 deviations (σ) above the background level. This is intended to discard isolated bright
 155 pixels. Inspection of all STIS images revealed six positive detections (out of twenty-six
 156 exposures, hence detections in roughly a quarter of exposures, strikingly similar to L12)
 157 displayed in Figure 2 a₁-f₁ (and replicated in Figure 2 a₂-f₂ with grids of planetocentric
 158 coordinates) and indicated by white arrows. These detections appear in three pairs of

consecutive images taken on 27 Sept. 2012, 1-2 and 24 Nov. 2014. The corresponding observing parameters are indicated in columns 1-5 of Table 1, which also includes the previous detections analyzed by L12 for comparison purposes. The peak intensity exceeded the 5σ level in images c_1 and f_1 , with $\sigma = 2.5$ kR of H_2 in average. The acquisition of STIS images in pairs further strengthens these detections since the auroral signal is seen to persist from one image to the next and to rotate with the planet. This motion is consistent with the expected $8 - 9^\circ$ longitudinal shift derived from the CML difference between two consecutive exposures.

Hereafter, longitudes refer to the Uranian Longitude System (ULS) [Ness *et al.*, 1986]. ULS longitudes are built from IAU-defined longitudes, both increasing with time, by referencing the 168.46° sub-Voyager 2 IAU longitude on 24 Jan. 1986 to 302° according to the ULS definition. Absolute longitudes cannot be determined any more as the reference has been lost, owing to the large uncertainty on the rotation period. From 24 Jan. 1986 to 24 Nov. 2014, the planet rotated 14660.3 ± 8.5 times. In the ULS system, latitude is measured positively from the equator toward the rotation axis and the northern and southern magnetic poles lie at $+15.2^\circ$ and -44.2° , respectively.

4.1. Morphology

These new auroral features display both strong similarities to and some differences from those detected in 2011. They appear as isolated spots, as in 2011, but with a larger spatial extent of up to several tens of pixels (1 pixel ~ 340 km). These emissions all lie in the southern hemisphere, nearly at the southern magnetic pole latitude, while the 2011 aurorae appeared closer to northern polar latitudes. Columns 6-7 of Table 1 provide the coordinates of the auroral peak and its spatial extent at half maximum, assuming an

181 auroral altitude at 1100km above the 1-bar level. This altitude is taken to be the same as
182 for Saturn's aurorae and is consistent with early models of peak auroral energy deposition
183 at Uranus [Waite *et al.*, 1988].

184 As noted above, the auroral spots appear to persist and rotate with the planet during
185 each pair of consecutive images. Quantitatively, Table 1 shows that the peak emission on 27
186 Sept. 2012 and 1-2 Nov. 2014 did not vary by more than 2° in latitude and 3° in longitude,
187 well within the extent of the auroral region. This suggests a single active region fixed in
188 longitude. In contrast, on 24 Nov. 2014, the peak emission remains at constant latitude
189 but shifts by 11° in longitude. This compares with the larger size of the auroral region
190 itself whose morphology (as well as intensity and dynamics, discussed below) significantly
191 evolves from the first image to the second.

192 Interestingly, the aurorae seen on 1-2 and 24 Nov. 2014, 22 days apart, appear at the
193 same latitude and longitude. This indicates that, assuming an arbitrary southern auroral
194 oval of constant size, the same portion of it was activated for different CML, as already
195 observed in the north on 16 and 29 Nov. 2011, 13 days apart. The 27 Sept. 2012 aurorae
196 were activated 10° southward of the 2014 emissions, and at longitudes which cannot be
197 compared to those of 2014 due to the large uncertainty in the ULS system ($\pm 106^\circ$ per
198 year).

4.2. Energetics

199 Figure 2 displays images in kR of unabsorbed H_2 emission over 70-180 nm. A supple-
200 mentary 16% average contribution of H Ly α [Broadfoot *et al.*, 1986] may be added to
201 obtain an exhaustive estimate of the total flux radiated by H and H_2 . Column 8 of Table
202 1 lists the H_2 auroral peak brightnesses, for the 2012 and 2014 campaigns but also for the

1998 and 2011 ones. These generally lie within a range of 5-15 kR. An exceptionally high value of 17-24kR was reached on 24 Nov. 2014. We note that, within each pair of observations, the second image systematically displayed a brighter signal. We attribute these changes to intrinsic auroral variability as the active region is clearly seen to simultaneously extend and brighten in each case. The brightnesses discussed above are roughly consistent with the few kR estimated by L12 for the 2011 auroral spots in the observed 25MAMA range, and they strikingly compare to (and in the case of 24 Nov. 2014 emissions even significantly exceed) the 9 kR of H₂ emission derived from Voyager 2/UVS measurements of southern nightside aurorae. Uranus aurorae are much less bright than Jupiter's but compare well with the average 10 kR of Saturn's aurorae (e.g. [Lamy et al., 2013, and references therein]).

To estimate the total radiated power, we derived the total number of counts per second within a constant radius circle encompassing the auroral signals (17 pixels \sim 5800 km). This size was chosen by fitting the largest spot in figure 2f₁ and then applied to all the images for the sake of consistency (except for the 1998 observation which displayed auroral features of different shape and wider than 17 pixels). Values were then converted into total H₂ power as described in section 3. The results are provided in column 9 of Table 1 (except for figure 2d₁ which was contaminated by an irregular glow on the detector preventing any reliable power estimate). The large associated uncertainty has been estimated separately for each image. This uncertainty divides into \sim 1/3 of Poisson noise and \sim 2/3 of error on the background. The resulting power ranges from 1.3 ± 1.0 GW on 1 Nov. 2014 to 8.8 ± 1.8 GW on 24 Nov. 2014. Assuming the canonical 10% efficiency between precipitated and radiated power, the precipitated power ranges from 13 to 88 GW.

226 The radiated powers again compare with (as for brightnesses) but here do not exceed the
227 $\sim 6\text{-}14$ GW inferred from Voyager 2/UVS measurements of southern nightside aurorae.
228 This likely results from emissions less spatially extended near equinox than at solstice.
229 Similarly, such values remain lower than the usual power radiated by Saturn's aurorae,
230 which extend along wide, circumpolar ovals.

4.3. Dynamics

231 The auroral dynamics appears to differ slightly from what was observed in 2011. The
232 latter were seen to vary on timescales of minutes. Here, the auroral signatures persist
233 over longer intervals, covered by two consecutive images. From the delay between the
234 mid-exposure times of consecutive images, the active region lasts for at least ~ 17 , 18 and
235 13 min on 27 Sept. 2012, 1-2 and 24 Nov. 2014, respectively. Within these active periods,
236 variations and recurrences can be observed on much shorter timescales.

237 To investigate this dynamics in more details, we performed a time-tag analysis of the
238 brightest auroral features seen on 24 Nov. 2014. The time-tag mode enables us to process
239 the data at the desired time resolution and to build time series of the counts recorded
240 in a specific region of the detector. The auroral signal detected on 24 Nov. 2014 was
241 sufficiently high to motivate the analysis of its temporal dynamics over the exposure
242 time of the two images displayed in figures 2e₁ (clear filter 25MAMA) and 2f₁ (filter
243 F25SrF₂). As reminded in table 1, these images were acquired successively at 08:34: 22
244 and 09:04:00 UT (Earth time) and integrated over 757 s and 900 s respectively. The lower
245 effective integration time of the former 25MAMA image (compared to other F25SrF₂
246 or 25MAMA images) is due to an unusually high count rate dominated by geocoronal

247 contamination which, in turn, saturated the onboard buffer memory before the data could
248 be transferred, resulting in several significant data gaps.

249 Figure 4 replicates figures 2e₁-f₁. On top of each image, four 17 pixels wide white
250 circles are drawn, defining four discs over each of which a count rate was derived. A disc
251 surrounding the auroral emission region (labelled S) was first used to determine the signal
252 count rate. The three other discs (labelled B₁ to B₃) were chosen out of the auroral region
253 at similar solar zenithal angles across the planet, with B₁ being additionally chosen at the
254 same latitude as S. The signal averaged over discs B₁-B₃ served to determine a background
255 count rate with a low noise. Time series of the difference between the signal and the
256 background count rate are displayed below each image of Figure 4 with three different
257 temporal resolutions : 1 s, 2 s and 10 s from top to bottom respectively. Hereafter, we
258 pay specific attention to episodes which reached or exceeded 2 or 3 standard deviations
259 σ above the background level (indicated by horizontal dashed and dashed-dotted lines
260 respectively), although the σ reference may be slightly over-estimated due to the presence
261 of auroral emission.

262 Although the 25MAMA image was built over discontinuous intervals, the 10 s integrated
263 histogram clearly displays 4 peaks in excess of 3σ during the first minute of integration.
264 The 10 s integrated histogram corresponding to the F25SrF₂ image displays 3 recurrent
265 peaks of auroral signal beyond 3σ until 14 minutes after the start of the exposure. These
266 peaks are statistically significant, as a random gaussian distribution of the same number
267 of points shall result in 0.23 and 0.27 data points respectively with an amplitude in excess
268 of 3σ above the mean level. Taken altogether, these results give evidence that the auroral
269 region was active during at least 36 min, which increases our above first, rough, 13 min

estimate. A closer inspection of the right-handed histograms, which were built from the
brightest Uranus auroral emission ever seen with HST (see table 1), provides further
information on the auroral short-term dynamics. The 10 s integrated histogram shows 3
auroral bursts above 3σ and 3 more reaching 2σ , which repeat along the interval, spaced
by several minutes. These bursts are brief and made of individual pulses lasting for less
than 1-2 s. The 1 s integrated histogram for instance displays 15 pulses at or in excess of
the 3σ level (while a gaussian distribution predicts that only 2.7, hence 3 data points shall
randomly reach this level) and many more at the 2σ level. The Fourier transform of the
1 s integrated histogram (not shown) displays several peaks of moderate amplitude, the
most intense one being at 2.5 min (secondary peaks are visible at 0.1, 0.45 and 1.3 min).
This 2.5 min recurrence is tentatively indicated with double arrows on the 10 s integrated
histogram. While the reliability of this quasi-period deserves to be confirmed over a
more statistical dataset, it is interesting to note that similar quasi-periodic polar auroral
flares with timescales of several minutes, attributed to dayside pulsed reconnection, have
similarly been observed at Earth and Jupiter [Bonfond *et al.*, 2011, and refs therein].

4.4. Localization of magnetic poles

In Figure 2, model southern auroral ovals are displayed in red (the associated blue
northern ovals are not visible as they are located on the nightside). They were derived from
the most up-to-date AH5 magnetic field model of Uranus [Herbert, 2009] and delimited
by a pair of solid lines which map the footprints of magnetic field lines whose apex reaches
5 (outer line) and 20 (inner line) Uranian radii respectively ($1 R_U = 25559$ km) at the
1100 km altitude. This wide interval provides a fair guide to investigate any auroral field
lines, as it encompasses most of the inner magnetosphere (the 1986 aurorae lay at the

292 footprint of AH5 field lines of apex just outside $5 R_U$) and the outer magnetosphere (the
293 sub-solar standoff distance of the magnetopause lay at $18 R_U$ during the Voyager 2 flyby,
294 and is likely to be less during magnetospheric compressions).

295 In order to quantitatively constrain the longitude of the magnetic poles, we have built a
296 composite cylindrical brightness map from all the 2014 images, including those which did
297 not exhibit any significant auroral signal to take into account any possible weak or diffuse
298 additional aurorae not investigated above. The result is displayed on figure 3. As a result
299 of the planetary inclination, the projection maps all longitudes, and latitudes $\leq 50^\circ$. We
300 then built a mask from model auroral ovals defined above, and performed a 2D cross-
301 correlation between the two projections by shifting the mask in longitude. This assumes
302 that the latitude of magnetic poles had not varied since 1986. The correlation coefficient
303 clearly peaks twice at 0.15 and 0.13, above an average level of 0.05, for longitudes of the
304 southern magnetic pole of 104° and 118° , respectively. We chose the first peak as best fit,
305 and used it to fix the longitude of both magnetic poles. The corresponding model ovals
306 are overplotted on the data in figure 3. The existence of a second peak of comparable
307 (although lower) amplitude simply illustrates that the aurorae, mainly clustered around
308 one localized active region, cannot be uniquely fitted : the oval corresponding to the
309 second fit is located to the right on figure 3. The half maximum of the highest correlation
310 coefficient yields a conservatively acceptable range of $78\text{-}130^\circ$ longitude. Therefore, we
311 identify the southern (northern) magnetic pole at $104 \pm 26^\circ$ ($284 \pm 26^\circ$) longitude over the
312 month of Nov. 2014. The subsequent update of the rotation period and ULS system using
313 the full set of HST auroral detections is beyond the scope of this paper.

314 A similar approach could not be applied to the 2012 observations, because of less fre-
315 quent and weaker auroral emissions. The model ovals displayed in figures 2a₂-b₂ thus
316 simply indicate a visual best fit.

5. Discussion

317 The six detections acquired from the 2012 and 2014 HST campaigns now add to the
318 three auroral signatures detected during the 1998 and 2011 HST campaigns. Although the
319 statistics remain limited, this collection nonetheless provides a basis to further investigate
320 possible origins for the observed auroral precipitations.

321 The ring-like faint emissions of 1998 were discussed by L12 who proposed that they are
322 powered by some magnetospheric acceleration process, active for an intermediate Solstice-
323 to-Equinox configuration, and able to operate over a wide range of longitudes. This is
324 consistent with the particularly quiet solar wind conditions which prevailed for more than
325 5 days on both sides of the observations (Figure 1a).

326 From the persistent localized and dynamic nature of auroral spots observed over the
327 2011-2014 period on the sunlit hemisphere, post-Equinox Uranus aurorae are a good can-
328 didate for cusp emission (as observed at the Earth, Jupiter and Saturn) at or near the
329 boundary between open and closed field lines. The detected aurorae are brief, second-
330 long events, modulated on timescales of minutes and lasting several tens of minutes. L12
331 already proposed that the 2011 auroral spots could result from impulsive plasma injec-
332 tions through dayside reconnection with the interplanetary magnetic field, expected to
333 be favored once per rotation according to the variable solar wind/magnetosphere geom-
334 etry. Interestingly, the 2011 and 2014 auroral features were in each case radiated by a
335 region which, although activated several weeks apart, remained strikingly fixed in lati-

336 tude and longitude. If we assume that the aurorae are related to dayside reconnection, a
337 fixed emission locus would therefore suggest a stable reconnection site, in contrast with
338 the expectations of *Masters* [2014]. We note, however, that such a mapping is generally
339 poorly reliable due to the complex topology of magnetic field lines at the magnetospheric
340 cusps. Furthermore, *Cowley* [2013] pointed out that the topology of magnetic field lines
341 wound around the planet by the rotation is likely to be complex and may even prevent
342 dayside reconnection part of the time. Whether injections are triggered by dayside or
343 nightside reconnections cannot be inferred without a better knowledge of the planetary
344 field geometry.

345 Further information on any influence of the solar wind is provided by figure 1, which
346 indicates all the HST detections with gray arrows plotted over the interplanetary dynamic
347 pressure, where the size of the arrow is qualitatively proportional to the signal strength.
348 Despite the large $\sim \pm 3$ days uncertainty in the arrival time, this global view draws gen-
349 eral trends. We first note that the 2014, 2011 (and even 2012) positive detections match
350 episodes of globally enhanced solar wind activity - as consistently predicted by the dif-
351 ferent MHD models - lasting for several days and made of successive individual pressure
352 fronts. The most intense Uranus aurorae ever observed (24 kR, 8.8 GW) interestingly
353 match a high-pressure episode ($P \geq 0.017 \text{ nPa}$ for 2 models over 3), the largest ever sam-
354 pled at Uranus. While the solar wind is known as a driver for part of planetary aurorae in
355 general, it is worth noting that terrestrial cusp aurorae brighten in particular during mag-
356 netospheric compressions, their location being controlled by the interplanetary magnetic
357 field orientation [*Farrugia et al.*, 1995]. Possible Uranian cusp aurorae discussed above
358 might thus be similarly triggered by solar wind compressions.

359 On the other hand, the limited number of positive detections over all the HST obser-
360 vations which sampled long-lasting periods of active solar wind suggests that the Uranus
361 aurorae also likely depend on the planetary field geometry, and therefore on the planetary
362 rotation, as the mean interplanetary magnetic field at 19 AU remains almost entirely
363 azimuthal.

6. Conclusion

364 In this article, we analyzed two HST/STIS imaging campaigns of Uranus acquired in
365 2012 and 2014 with different temporal coverage under variable solar wind conditions.
366 Their analysis yielded the identification of six additional detections of Uranus' aurorae
367 acquired on 27 Sept. 2012, 1-2 and 24 Nov. 2014. The persistence of auroral signal
368 on consecutive images at the same coordinates provides direct evidence of a rotational
369 motion with the planet. The aurorae were localized from -50° (in 2012) to -40° (in 2014)
370 southern latitudes. The auroral regions of 1-2 and 24 Nov. 2014 were also rotationally
371 phased, which suggests that the same portion of any auroral oval was activated 22 days
372 apart, as in 2011. The detected emissions lasted for tens of minutes. The auroral region
373 of 24 Nov. 2014 was active for at least 36 min and composed of brief pulses of emission,
374 lasting for less than 1-2s and variable on timescales of minutes, with a main recurrence
375 period of ~ 2.5 min.

376 The auroral spots radiated 5-24 kR and 1.3-8.8 GW, which are comparable to the inten-
377 sity of Uranian aurorae observed previously and demonstrate that these can be routinely
378 observed with HST (the four investigated campaigns each included at least one detection).
379 The Nov. 2014 observations were fitted with model auroral ovals which constrained the
380 longitude of the southern (northern resp.) magnetic pole to $104 \pm 26^\circ$ ($284 \pm 26^\circ$ resp.)

381 ULS. We suggest that near-equinoctial Uranus aurorae might be pulsed cusp emissions
382 formed by either dayside or nightside reconnection. The time (and possible amplitude)
383 correlation between aurorae and sudden increases of solar wind dynamic pressure may
384 suggest a prominent influence of the solar wind for driving auroral precipitation (to be
385 confirmed), in addition to the planetary field geometry. These results form a basis for fur-
386 ther modeling work of magnetic reconnection or full solar wind/magnetosphere interaction
387 using realistic solar wind parameters prevailing during the investigated observations.

388 The comparative analysis of Uranus' aurorae detected by HST over 16 years shows an
389 overall variation of Uranus auroral properties from a Solstice-to-Equinox situation (1998)
390 to a configuration gradually moving away from Equinox (2011 to 2014). It is essential
391 to pursue observing Uranian aurorae with HST, the most powerful FUV telescope in
392 activity, as the intermediate Equinox-to-Solstice configuration will be reached in 2017.
393 This configuration will provide an opportunity to check the single auroral detection of 1998
394 under various solar wind conditions and identify the associated magnetospheric dynamics.
395 Neptune, which forms the family of ice giants planets with Uranus, also represents a
396 worthy unexplored target whose aurorae are likely accessible to HST sensitivity. Neptune's
397 magnetosphere is less tilted with denser and longer plasma residence times, and may thus
398 respond to the solar wind in a similar fashion as Uranus does.

Appendix A: Solar wind propagation models

A1. mSWiM

399 The mSWiM 1D model considers the solar wind as an ideal MHD fluid propagated from
400 spacecraft in situ measurements at 1 AU outward in the solar system in a spherically
401 symmetric configuration. The model was originally developed and extensively validated

402 for propagation to between 1 and 10 AU [*Zieger and Hansen, 2008*] (1 AU = 1 astronomical
 403 unit). The input boundary conditions at 1 AU are rotated to an inertial longitude.
 404 Propagation occurs at the inertial longitude and then results are rotated to the target
 405 body. Motion of the both the spacecraft providing the boundary conditions and the
 406 target body are taken into account. As expected, the model provides the most accurate
 407 results when the sun-spacecraft-target are aligned in heliographic longitude. Both the L12
 408 study and the present one use a modified version of this code where the mass loading due
 409 to interstellar neutrals in the outer heliosphere (10-20 AU) is taken into account.

A2. Tao model

410 The Tao 1D model considers the solar wind as an ideal MHD fluid in a one-dimensional
 411 spherical symmetric coordinate system. The equation set, numerical scheme, model set-
 412 ting, and inputs are detailed in [*Tao et al., 2005*]. The modifications brought to the code
 413 to propagate solar wind up to the Uranus orbit are described below.

414 To account for the effect of the solar rotation, the solar wind arrival time is delayed by
 415 $\Delta t = \Delta\Phi/\Omega$, where $\Delta\Phi$ is the Earth-Sun-Uranus angle and Ω is the solar angular velocity
 416 (using a 26 days rotation period).

417 In the outer heliosphere (beyond 10 AU), the interaction between the solar wind and
 418 the neutral hydrogen of the local interstellar medium becomes non-negligible. It is taken
 419 into account by assuming that the neutral hydrogen distribution and the temperature
 420 vary as a function of the heliospheric distance r as follows.

421 The hydrogen density $n_H(r)$ and velocity $u_H(r)$ are defined as in [*Wang and Richard-*
 422 *son, 2001*] (equation 7) : $n_H(r) = n_H^\infty \exp^{-\lambda/r}$ and $u_H(r) = u_H^\infty$ with $\lambda = 7.5$ AU,
 423 $n_H^\infty = 0.09 \text{ cm}^{-3}$ [*Wang and Richardson, 2003*] and $u_H^\infty = 20 \text{ km/s}$. The direction of

424 the interstellar wind is used to derive the radial and azimuthal components of the velocity
 425 along the the Sun-Uranus reference line [*Lallement et al.*, 2010].

426 The temperature profile is defined as in [*Wang and Richardson*, 2003] : $T_H(r) = 1000 +$
 427 $T_H^\infty \exp^{-\lambda/r}$, where $T_H^\infty = 1.09 \times 10^4$ K.

428 The interaction of the solar wind with the neutral hydrogen is introduced through the
 429 momentum and energy equations following the description of *McNutt et al.* [1998] (see
 430 equations 29, 70 and 71). The energy source term is multiplied by 1.8 in order to obtain
 431 a steady state proton temperature profile consistent with Voyager 2 observations (e.g.
 432 Figure 1 of [*Wang and Richardson*, 2003]).

A3. MS-FLUKSS

433 *Kim et al.* [2016] recently developed a 3D model which predicts solar wind conditions
 434 between 1 and 80 AU from time-dependent boundary conditions implemented in the
 435 adaptive mesh refinement framework of Multi-scale Fluid-kinetic Simulation Suite (MS-
 436 FLUKSS), which is a numerical toolkit designed primarily for modeling flows of partially
 437 ionized plasma (see [*Pogorelov et al.*, 2014, and refs therein]). MS-FLUKSS solves MHD
 438 equations for plasma coupled either with the kinetic Boltzmann or multiple gas dynamics
 439 Euler equations describing the flow of different populations of neutral atoms. Several
 440 different turbulence models are implemented in MS-FLUKSS together with different ap-
 441 proaches to treat non-thermal (pickup) ions as a separate plasma components. In this
 442 particular simulation, the model takes into account the effects of pickup ions that are
 443 created in the charge-exchange process between the solar wind and interstellar neutral
 444 atoms. While the flows of plasma and neutral atoms are described separately by solving
 445 the MHD and Euler equations, respectively, the thermal (solar wind) and non-thermal

(pickup ions) plasma are treated as a single, isotropic fluid. Thus, the model plasma temperatures are generally greater than those expected for the solar wind at distances greater than ~ 10 AU such as at Uranus, due to the contribution from the much hotter pickup ions that become increasingly dominant at larger distances.

A4. Comparison of the model predictions at Uranus

As only the MS-FLUKKS results have been validated yet in the outer heliosphere, these results are hereafter taken as a reference to which the mSWiM and Tao results are compared to assess typical uncertainties.

The solar wind parameters at Uranus predicted by these three models are compared on Figure 5 throughout a representative time interval of 66 days, which encompasses the Nov. 2014 HST observations. The most accurately propagated parameters are the radial velocity (top panel) and the density (middle panel), or their combination within the dynamic pressure (bottom panel), whose sudden increases indicate interplanetary shocks. Results from MS-FLUKKS, mSWiM and the Tao model and MS-FLUKKS are displayed in orange, black and blue, respectively.

Figure 5 illustrates a general agreement between the results of the three models which all predict three different disturbed solar wind episodes separated by three quiet conditions episodes. We note that mSWiM's densities are generally lower than those of MS-FLUKKS and Tao. In addition, these densities remain strikingly low and constant after DOY 320, while the mSWiM's densities calculated without considering interstellar neutrals (not shown) are more consistent with MS-FLUKKS's and Tao's ones during this period. The mSWiM's predictions are thus considered as insufficiently reliable after day 320 of year 2014.

468 The delay between the arrival of velocity, density or pressure fronts predicted by the
469 three models varies from 1 to 5 days, from 2 to 5 days and from 2 to 4 days during
470 the three active solar wind periods (DOY 284-292, 298-309 and 323-331, respectively).
471 Consequently, we have set an estimate of ± 3 days uncertainty, as indicated in the main
472 text. However, many individual fronts apparent in Figure S1 (late 2014) and most of
473 the fronts displayed in Figure 1 (mid 1998, late 2011, late 2012) display a much better
474 coincidence.

475 **Acknowledgments.** This work is based on observations of the NASA/ESA Hubble
476 Space Telescope (Programs GO #13012 and GO/DD #14036). We thank the Space
477 Telescope Science Institute staff for their support in scheduling the observations. The
478 French co-authors acknowledge support from CNES and thank L. Gosset who worked on a
479 preliminary analysis of the 2014 data during a master internship in 2015. We acknowledge
480 the APIS service <http://apis.obspm.fr>, hosted by the Paris Astronomical Data Centre, and
481 regularly used to browse and investigate the data, and thank in particular F. Henry and
482 P. Le Sidaner who maintain this service. We acknowledge use of NASA/GSFC's Space
483 Physics Data Facility's OMNIWeb service <http://omniweb.gsfc.nasa.gov> and OMNI data.
484 We thank the CCMC and L. Mays to have ran the ENLIL model specifically at Uranus for
485 comparison purposes. Work at Leicester was supported by STFC grant ST/N000749/1.
486 SVB was supported by STFC Fellowship ST/M005534/1. TK and NP were supported by
487 NASA grants NNX14AF41G and NNX14AJ53G, and NSF SHINE grant AGS-1358386.

Notes

488 1. http://www.stsci.edu/hst/HST_overview/instruments

References

- 489 Arridge, C. S., et al. (2011), Uranus Pathfinder: exploring the origins and evolution of Ice
 490 Giant planets, *Experimental Astronomy*, p. 113, doi:10.1007/s10686-011-9251-4.
- 491 Barthélémey, M., et al. (2014), Dayglow and auroral emissions of Uranus in H₂ FUV bands,
 492 *Icarus*, *239*, 160–167, doi:10.1016/j.icarus.2014.05.035.
- 493 Bonfond, B., et al. (2011), Quasi-periodic polar flares at Jupiter: A signature of pulsed
 494 dayside reconnections?, *Geophys. Res. Lett.*, , *38*, L02104, doi:10.1029/2010GL045981.
- 495 Broadfoot, A. L., et al. (1986), Ultraviolet spectrometer observations of Uranus, *Science*,
 496 *233*, 74–79, doi:10.1126/science.233.4759.74.
- 497 Cowley, S. W. H. (2013), Response of Uranus' auroras to solar wind compressions
 498 at equinox, *Journal of Geophysical Research (Space Physics)*, *118*, 2897–2902, doi:
 499 10.1002/jgra.50323.
- 500 Farrugia, C. J., et al. (1995), Reconnection-associated auroral activity stimulated by two
 501 types of upstream dynamic pressure variations: Interplanetary magnetic field $B_z \sim 0$,
 502 $B_y \ll 0$ case, *J. Geophys. Res.*, , *100*, 21,753–21,772, doi:10.1029/95JA01082.
- 503 Gustin, J., et al. (2012), Conversion from HST ACS and STIS auroral counts into bright-
 504 ness, precipitated power, and radiated power for H₂ giant planets, *Journal of Geophys-*
 505 *ical Research (Space Physics)*, *117*, A07316, doi:10.1029/2012JA017607.
- 506 Herbert, F. (2009), Aurora and magnetic field of Uranus, *Journal of Geophysical Research*
 507 *(Space Physics)*, *114* (A13), A11206, doi:10.1029/2009JA014394.
- 508 Herbert, F., and B. R. Sandel (1994), The Uranian aurora and its relationship to the
 509 magnetosphere, *J. Geophys. Res.*, , *99*, 4143–4160, doi:10.1029/93JA02673.
- 510 Kim, T. K., et al. (2016), Modeling the Solar Wind at the Ulysses, Voyager, and New Hori-

- 511 zons Spacecraft, *Astrophysical Journal*, *32*(1), 72, doi:10.3847/0004-637X/832/1/72.
- 512 Lallement, R., et al. (2010), The Interstellar H Flow: Updated Analysis of
513 SOHO/SWAN Data, *Twelfth International Solar Wind Conference*, *1216*, 555–558, doi:
514 10.1063/1.3395925.
- 515 Lamy, L., et al. (2012), Earth-based detection of Uranus' aurorae, *Geophys. Res. Lett.*, ,
516 *39*, L07105, doi:10.1029/2012GL051312.
- 517 Lamy, L., et al. (2013), Multispectral simultaneous diagnosis of Saturn's aurorae through-
518 out a planetary rotation, *Journal of Geophysical Research (Space Physics)*, *118*, 4817–
519 4843, doi:10.1002/jgra.50404.
- 520 Masters, A. (2014), Magnetic reconnection at Uranus' magnetopause, *Journal of Geo-*
521 *physical Research (Space Physics)*, *119*, 5520–5538, doi:10.1002/2014JA020077.
- 522 McNutt, R. L., Jr., et al. (1998), Simulation of the heliosphere - Model, *J. Geophys. Res.*,
523 , *103*, 1905, doi:10.1029/97JA02143.
- 524 Ness, N. F., et al. (1986), Magnetic fields at Uranus, *Science*, *233*, 85–89, doi:
525 10.1126/science.233.4759.85.
- 526 Pogorelov, N. V., et al. (2014), MS-FLUKSS and Its Application to Modeling Flows of
527 Partially Ionized Plasma in the Heliosphere, in *2014 Annual Conference on Extreme*
528 *Science and Engineering Discovery Environment*, ACM Digital Library (New York),
529 doi:doi:10.1145/2616498.2616499.
- 530 Tao, C., et al. (2005), Magnetic field variations in the Jovian magnetotail induced by
531 solar wind dynamic pressure enhancements, *Journal of Geophysical Research (Space*
532 *Physics)*, *110*(A9), A11208, doi:10.1029/2004JA010959.
- 533 Vincent, M. B., et al. (2000), Mapping Jupiter's Latitudinal Bands and Great

- 534 Red Spot Using HST/WFPC2 Far-Ultraviolet Imaging, *Icarus*, *143*, 189–204, doi:
535 10.1006/icar.1999.6232.
- 536 Waite, J. H., Jr., et al. (1988), Superthermal electron processes in the upper atmo-
537 sphere of Uranus - Aurora and electroglow, *J. Geophys. Res.*, , *93*, 14,295–14,308,
538 doi:10.1029/JA093iA12p14295.
- 539 Wang, C., and J. D. Richardson (2001), Energy partition between solar wind protons and
540 pickup ions in the distant heliosphere: A three-fluid approach, *J. Geophys. Res.*, , *106*,
541 29,401–29,408, doi:10.1029/2001JA000190.
- 542 Wang, C., and J. D. Richardson (2003), Determination of the solar wind slowdown
543 near solar maximum, *Journal of Geophysical Research (Space Physics)*, *108*, 1058, doi:
544 10.1029/2002JA009322.
- 545 Zieger, B., and K. C. Hansen (2008), Statistical validation of a solar wind propagation
546 model from 1 to 10 AU, *Journal of Geophysical Research (Space Physics)*, *113*(A12),
547 A08107, doi:10.1029/2008JA013046.



Figure 1. Solar wind dynamic pressure at Uranus predicted by three MHD models (described in appendix 3.3) for the HST campaigns of (a) 1998, (b) 2011, (c) 2012 and (d) 2014. The uncertainty on pressure fronts is estimated to ± 3 days. Vertical gray lines mark the distribution of HST orbits using STIS (solid), ACS (dashed) and COS (dotted) instruments. Gray arrows indicate positive auroral detections with a size qualitatively proportional to their intensity.

D R A F T

March 7, 2017, 9:31pm

D R A F T

Date (Earth time)	Dataset	Filter	Exposure	CML	Latitude	Longitude	Peak brightness	Total Power
1998-07-29 06:07:43 UT	o4wt01t0q	25MAMA	1020s	180°	$35 \pm 35^\circ$	$93 \pm 23^\circ$	4 kR	–
2011-11-16 15:32:10 UT	obrx10p0q	25MAMA	1020s	338°	$11 \pm 3^\circ$	$49 \pm 5^\circ$	11 kR	2.0 ± 0.8 GW
2011-11-29 02:09:24 UT	obrx18hbq	25MAMA	1020s	93°	$9 \pm 3^\circ$	$55 \pm 3^\circ$	10 kR	2.4 ± 0.8 GW
2012-09-27 15:00:19 UT	obz501dgq	25MAMA	1250s	296°	$-50 \pm 3^\circ$	$297 \pm 11^\circ$	5 kR	1.9 ± 1.3 GW
2012-09-27 15:27:07 UT	obz501diq	F25SrF ₂	820s	304°	$-49 \pm 4^\circ$	$294 \pm 11^\circ$	15 kR	2.2 ± 1.8 GW
2014-11-01 23:57:33 UT	ocpl02nzq	25MAMA	1231s	111°	$-40 \pm 4^\circ$	$105 \pm 7^\circ$	6 kR	1.3 ± 1.0 GW
2014-11-02 00:26:11 UT	ocpl02o6q	F25SrF ₂	900s	120°	$-38 \pm 4^\circ$	$105 \pm 13^\circ$	15 kR	–
2014-11-14 08:34:22 UT	ocpl07ckq	25MAMA	757s	155°	$-44 \pm 9^\circ$	$105 \pm 15^\circ$	17 kR	5.9 ± 1.4 GW
2014-11-14 09:04:00 UT	ocpl07cmq	F25SrF ₂	900s	165°	$-42 \pm 10^\circ$	$115 \pm 10^\circ$	24 kR	8.8 ± 1.8 GW

Table 1. (Columns 1 to 5) HST observing parameters at mid-exposure. (Columns 6 to 9) Properties of auroral emissions detected by HST in 1998, 2011, 2012 and 2014.



Figure 2. HST/STIS images acquired on 27 Sept. 2012 (a₁-b₁), 1-2 and 24 Nov. 2014 (c₁-f₁) and replicated with grids of planetocentric coordinates (a₂-f₂). Images were acquired with the 25MAMA (first column) and the F25SrF₂ (third column) filters and processed as described in the main text. They are displayed in kR of unabsorbed H₂ emission over 70-180 nm. The observing times are in Earth UT. White arrows indicate spatially extended bright spots above the detection threshold. The planetary configurations are corrected for light time travel (~ 2.7 hours). The dotted grey meridian marks the 0° ULS longitude. The red and blue dashed parallels (dotted-dashed meridians) mark the latitude (longitude) of the southern and northern magnetic poles, respectively. Model southern auroral ovals fitted to the data are displayed by pairs of solid red lines (see main text). The conjugate model northern auroral oval, shifted by 180° longitude, is not visible.

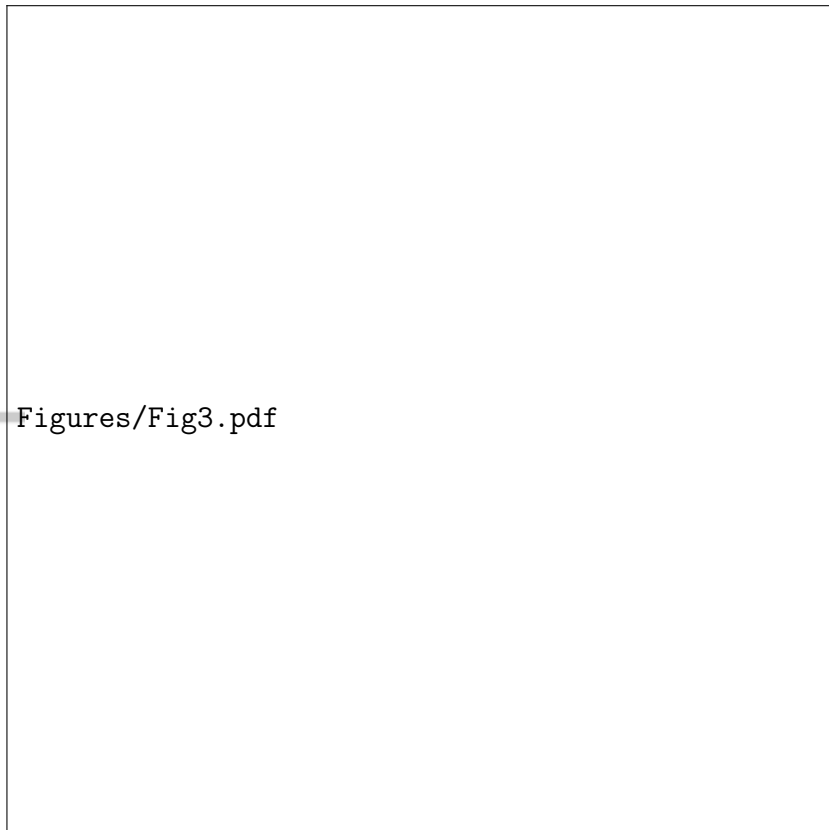


Figure 3. Composite cylindrical projection built from the 12 STIS processed images of Uranus obtained in Nov. 2014. The top white region indicates latitudes which could not be sampled. The average H_2 brightness was derived in $2^\circ \times 2^\circ$ bins. Uranocentric coordinates are taken at 1100 km above the 1-bar level. Red and blue pairs of solid lines indicate southern and northern model auroral ovals calculated with the AH5 model. Their outer and inner boundaries map the footprint of field lines whose apex reach 5 and 20 R_U respectively. The red and blue horizontal dashed parallels indicate the latitude of magnetic poles. The red and blue vertical dotted-dashed meridians indicate the best-fit longitude of magnetic poles, namely $104 \pm 26^\circ$ ($284 \pm 26^\circ$) for the southern (northern) pole.



Figures/Fig4.pdf

Figure 4. Consecutive images of Uranus acquired on 24 Nov. 2014 with the 25MAMA and F25SrF₂ filters. White circles define discs mapping regions with and without auroral emission. The disc labelled S surrounds the auroral region and served to determine the signal count rate. The discs labelled B₁, B₂ and B₃ surround background regions at similar solar zenithal angles, B₁ being additionally chosen at the same latitude as S. The signal averaged over discs B₁-B₃ served to determine a mean background count rate. The three histograms below each image display time series of the difference between the signal and the background count rate with different time resolution, namely 1 s, 2 s and 10 s from top to bottom respectively. Horizontal dashed and dashed-dotted lines indicate the 2 and 3 σ level above the background.

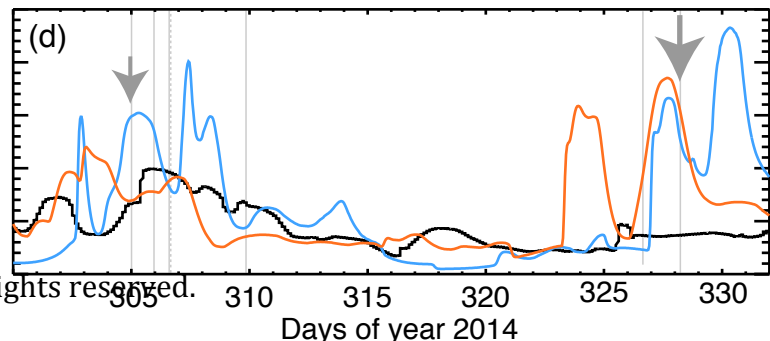
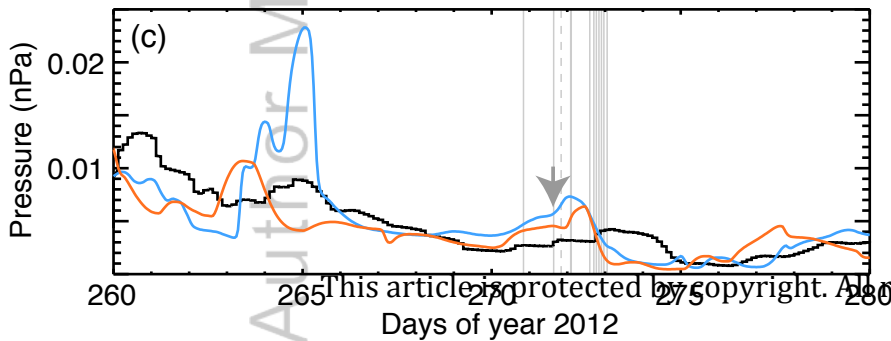
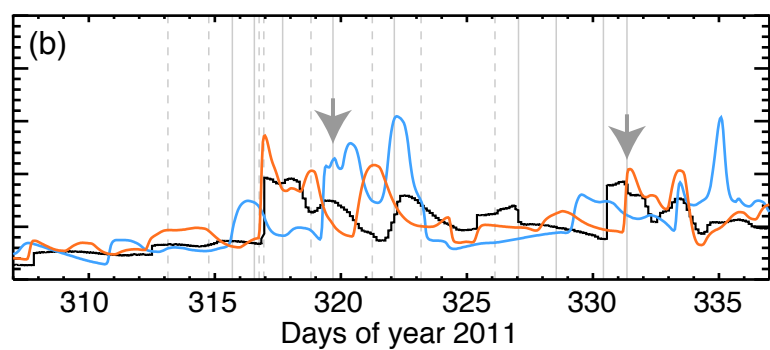
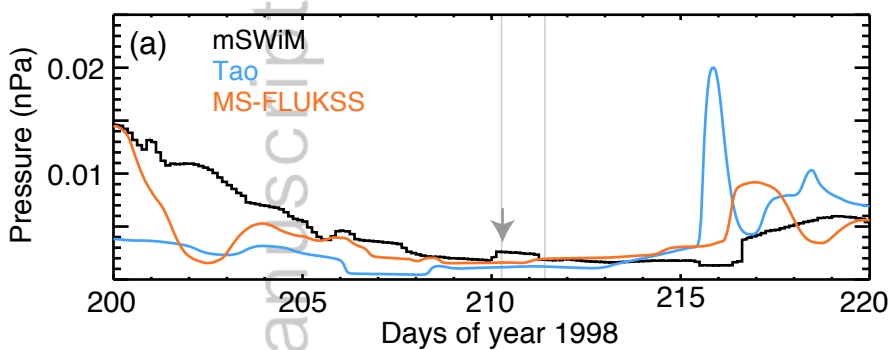
D R A F T

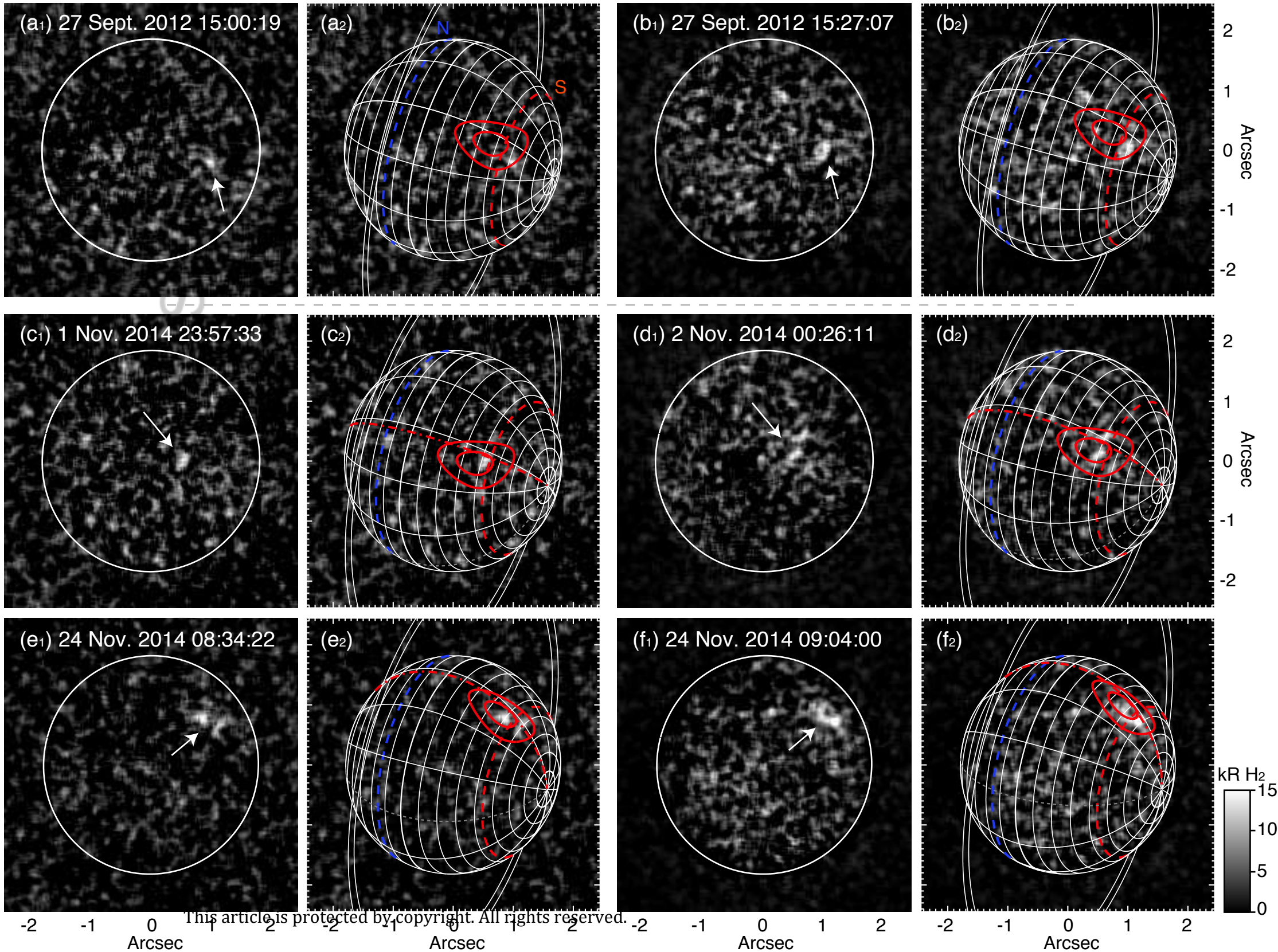
March 7, 2017, 9:31pm

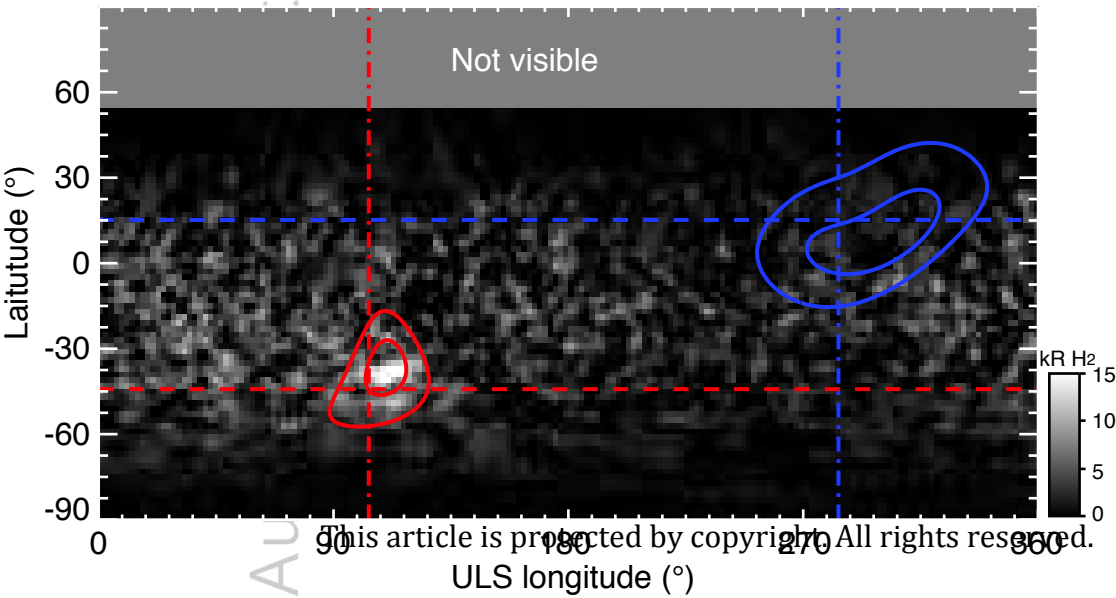
D R A F T

Figures/FigS1.pdf

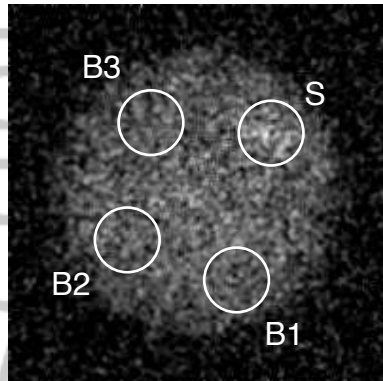
Figure 5. Solar wind velocity, density and dynamic pressure predicted at Uranus by the mSWiM (black), Tao (blue) and MS-FLUKSS (orange) models for late 2014.



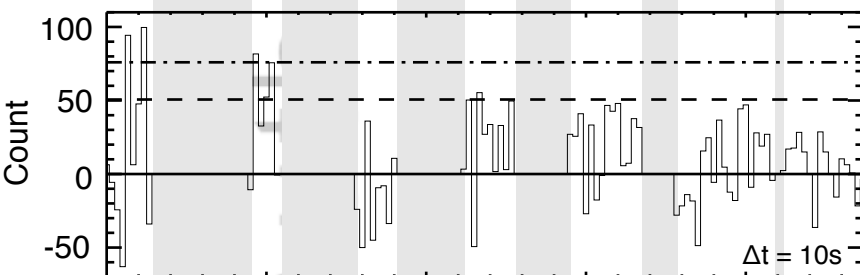
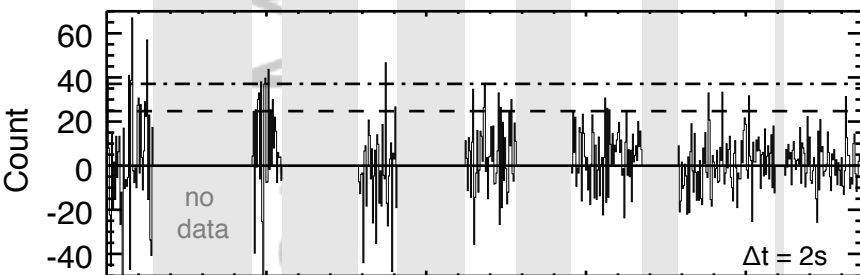
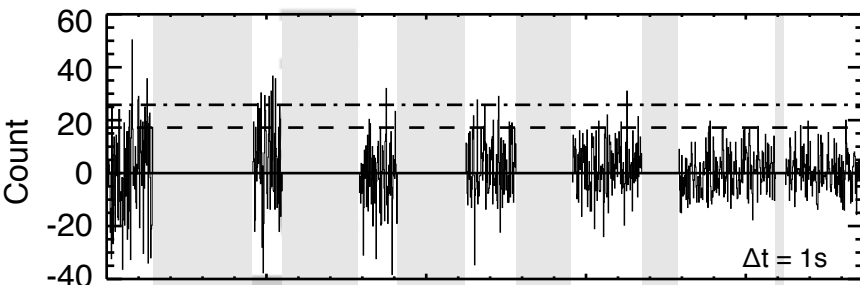
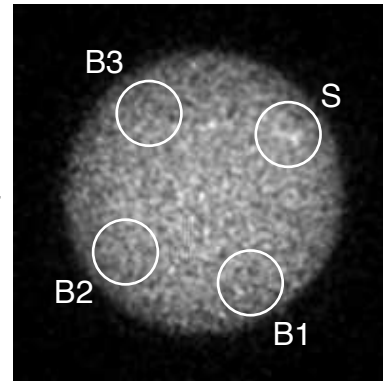




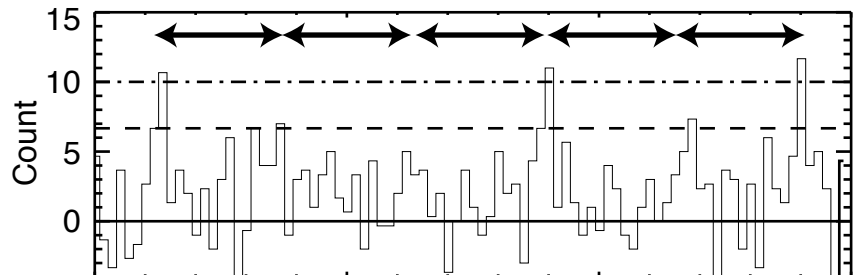
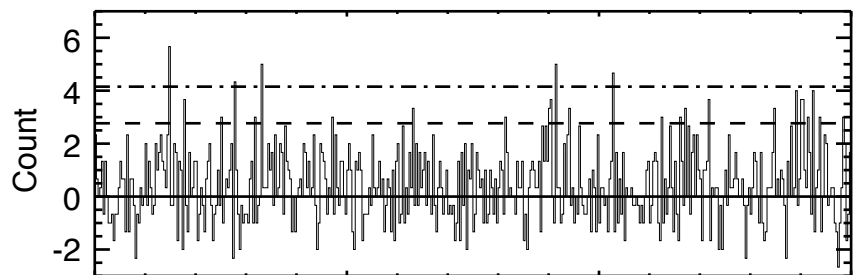
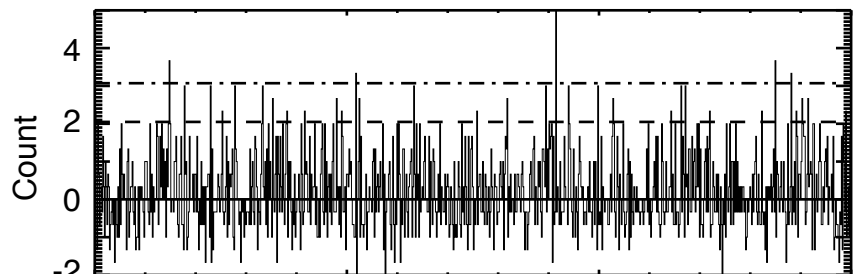
2014-11-14
08:34:22 UT
25MAMA



2014-11-14
09:04:00 UT
F25SrF2



5 10 15 20
Exposure time (min)



5 10 15
Exposure time (min)

